Materials Today Bio 29 (2024) 101256

Contents lists available at ScienceDirect

Materials Today Bio

journal homepage: www.journals.elsevier.com/materials-today-bio

Osteoinductivity enhancement by tailoring the surface chemical bond status: A strategy to mobilize host bone growth factors for *in situ* bone regeneration

Ruiyan Li [a], Kan Zhang [b,**], Chuanyao Dong [b], Kaiwen Wang [b], Xinlei Gu [b], Yanguo Qin [a,*]

[a] *Department of Orthopaedics, and Joint International Research Laboratory of Ageing Active Strategy and Bionic Health in Northeast Asia of Ministry of Education, The Second Hospital of Jilin University, Changchun, 130041, China*

[b] *State Key Laboratory of Super Hard Materials, Key Laboratory of Mobile Materials, MOE, School of Materials Science and Engineering, Jilin University, Changchun, 130012, China*

A R T I C L E I N F O

Keywords:
Endogenous regeneration
Reactive sputtering
Bone biomaterials
Bioactivity
Surface charge

A B S T R A C T

The incorporation of growth factors and biomaterials is a promising strategy for improving osseointegration. However, current strategies to develop biomaterials with exogenous growth factors present disadvantages like inefficiency, difficult deployment, and potential off-target activation, making their translation into clinical practice challenging. This study reveals a bioactive N-doped tantalum carbide (TaC) solid solution film that can be used to construct a TaCN film via bionic interface engineering to recruit host bone growth factors to the wounded site and improve bone regeneration. X-ray photoelectron spectroscopy (XPS) and protein absorption analysis reveal that the performance of TaCN is related to the surface chemical bonds of films. The introduction of N to TaC causes a cascade effect wherein negative charges enrich on the TaCN surface, and the recruitment of positively charged bone growth factors around the TaCN film is facilitated. Under these circumstances, the endogenous bone growth factors enhance bone healing. The TaCN film shows an outstanding performance for *in vivo* osteogenic differentiation along with a superior *in vitro* cytocompatibility. Incorporation of N atoms into TaC provides a new clinically translatable strategy to mobilize host bone growth factors for *in situ* bone regeneration without the need for incorporation of exogenous growth factors.

1. Introduction

The reconstruction of critical-sized bone defects has always been a difficult challenge in orthopedic practice and bone tissue engineering, and prosthesis implantation is the most common surgical therapy. Owing to the longer life expectancy of humans and substantial efforts to advance medical care, most patients live longer than the service life of their prostheses. For example, the lifetime risk of revision after total replacement of the hip or knee was increased for younger patients; up to 35 % for men in their early 50s [1]. Prostheses with weak osseointegration would lead to revision surgery, which is a growing burden for global public health and finances [2,3]. The most effective therapeutic strategy to achieve better osseointegration is to develop tissue engineering materials using relevant scaffolds, appropriate exogenous growth factors (GFs), and/or cells [4–6]. However, exogenous growth factor or cell delivery also leads to complications like short half-life, immunogenic concerns, high cost, rapid degradation, and possible toxicity [7–9]. Moreover, full clinical practice transition is challenging because of several disadvantages, including the retention of biological activity, the complex disinfection process before surgery, difficult deployment in the operating room, and mass production with uniform quality [4,10]. Consequently, it is particularly challenging and important to develop ideal cell- and GF-free implants that can recruit host cells and/or GFs to promote bone regeneration [11,12].

Some previous reports showed excellent strategies to overcome the need for the addition of cells into scaffolds. For example, a cell-free 3D scaffold with miRNA-26a delivery was used to activate endogenous stem and progenitor cells to heal critical-size tissue defects [11]. Meanwhile,

* Corresponding author. Department of Orthopaedics, and Joint International Research Laboratory of Ageing Active Strategy and Bionic Health in Northeast Asia of Ministry of Education, The Second Hospital of Jilin University, Changchun, 130041, China.

** Corresponding author.

E-mail addresses: kanzhang@jlu.edu.cn (K. Zhang), qinyg@jlu.edu.cn (Y. Qin).

https://doi.org/10.1016/j.mtbio.2024.101256

Received 17 June 2024; Received in revised form 21 August 2024; Accepted 15 September 2024

Available online 19 September 2024

a nano silica-functionalized scaffold that promotes host mesenchymal stem cell (MSC) recruitment and enhances endogenous bone regeneration was reported [7]. Autologous body fluid contains many GFs, which are interspersed all over the body at a low local concentration. Therefore, achieving local enrichment of host GFs is a feasible strategy for tissue regeneration. For example, use of platelet-rich plasma is one of most common methods to enrich autologous GFs, and provides a concentration of platelet-derived GFs (PDGFs) and transforming growth factor-βs (TGFβs) obtained by sequestering and concentrating platelets via gradient density centrifugation [13,14]. However, autologous growth factor collection and storage are carried out *in vitro*, which increases the risk of infection and disease transmission [15]. Therefore, a safer and more effective strategy is required to recruit autologous GFs *in situ* without the risk of infection.

Surface charges have been identified as key factors in regulating the interaction between biomaterials and surrounding cells [16,17]. The generation of negative charges on the surface of implants attracts cations, followed by proteins and cells. This process promotes the functionality of osteoblast cells, aiding in matrix mineralization and subsequently enhancing metabolic activities for bone regeneration [18]. Recently, transition metal carbides (TMeC) film have been received great attention in the biomedical field. Their excellent properties, like good biocompatibility and osteoinductivity, high hardness, chemical inertness and corrosion resistance, make them very promising candidates for applications in orthopedic and dental fields [19–21]. In particular, the tantalum carbide (TaC), it has also been reported to possess outstanding hemocompatibility for osteoblast cells, and expect to improve implant osseointegration in clinics [22,23]. Recent reports have demonstrated the chemical bond status, surface roughness, structure, texture and hardness of the tantalum carbide films can be tailored by the process parameters [21,24]. Changes in chemical composition and geometric morphology can serve as biochemical factors and biophysical cues for regulating the differentiation conditions of stem cells [25]. It is known that the tantalum carbide always absorbs oxygen in the air, leading to self-oxidation reaction upon the surface [26]. The incorporation of nitrogen into the film would alter its self-oxidation reaction. The TaC_xN_y film exposed in neutral liquid environment could absorb O_2 and H_2O, yielding ammonium ions (NH_4^+) and hydroxide ion (OH^-), and then film became negatively charged [27]. The negatively charged surface of TaC_xN_y film would provide a platform for mobilizing host GFs *in situ*.

In this study, we sputtered tantalum carbide (TaC) films and tailored their surface chemical status by doping N atoms, and constructed negatively charged surface OH- groups, and aimed to mobilize the bone growth factors (BGFs) upon the TaCN film for good *in vitro* osteogenic differentiation and *in vivo* osseointegration (as described in Scheme 1). The benefits of this strategy are as follows: (1) It is an innovative approach to enhance the bioactivity of the TaC film by doping it with solute N atoms to adjust the surface chemical bond status; (2) The thin film provides a suitable surface that endows the implant with excellent biocompatibility and osteoinductivity; and (3) Excellent *in situ* bone regeneration can be achieved through the mobilization of host BGFs, without the incorporation of exogenous GFs.

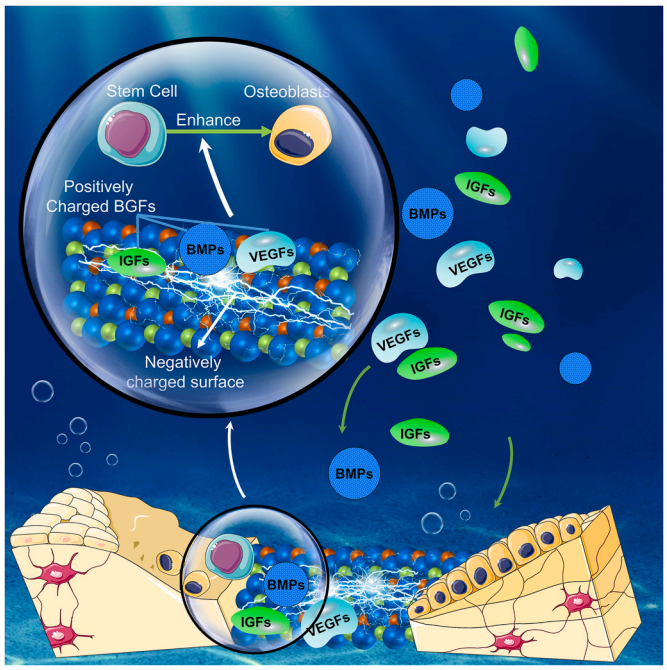

Scheme 1. Scheme showing the proposed mechanism of the mobilized host bone growth factors for *in situ* bone regeneration. (1) Most bone growth factors (BGFs) become positively charged in the body fluid; (2) negative charges enrich on the TaCN film surface, and the positively charged BGFs are recruited on the surface of the film; (3) BGFs on the film enhance the differentiation of bone stem cells.

2. Material and methods

2.1. Deposition of the films

TaC and TaCN films were deposited in a DC magnetron sputtering system using the TaC composite target (atomic ratio of Ta to C: ~1, purity: 99.95 %, Zhong Nuo Xin Cai Technology Co., Ltd, Beijing). Before sputtering, the background pressure ($<4 \times 10^{-4}$ Pa) was established using a turbomolecular Three substrates (Si(100) wafer, disk-shaped medical-grade Ti6Al4V (TC4) alloy $\Phi 10 \times 1.5$ mm in size, and TC4 screws $\Phi 3 \times 8$ mm in size) were selected for different measurements.TC4 disks and screws were purchased from Huitai metal materials Inc. Before sputter deposition, the TC4 substrates underwent consecutive polishing using silicon carbide papers down to 1200 grits, followed by ultrasonic cleaning in acetone, alcohol, and deionized water, and finally mounted on the substrate holder. To improve the film-substrate adhesion, we deposited a Ta layer onto the substrate before the deposition of TaC and TaCN films. During the deposition, the parameters of substrate bias temperature, voltage, target current, and working pressure were fixed at 200 °C, −80 V, 0.3 A, and 0.8 Pa, respectively. TaC films were deposited in Ar-containing atmosphere (80 sccm); to tailor the chemical states of TaC thin films, a mixed atmosphere of N_2 and Ar (30 sccm N_2/50 sccm Ar) was introduced. The deposition time was adjusted to achieve an optimum thickness of about 1.5–1.6 μm for all films.

2.2. Structure characterization

The structure of the films was characterized utilizing XRD with a Bragg-Brentano diffractometer (D8_tools) in θ-2θ configuration, using Cu Kα radiation and SAED (field emission JEOL 2100F). The composition and chemical bonds of the samples were characterized via XPS (ESCALAB-250) using Al Kα as the X-ray source at 2 keV. All samples were etched with Ar ion beam for 5 min in advance to remove surface oxides and determine accurate coating composition during the measurement. After SBF-soaking for 72 h, the surface bonding status of TaC and TaCN films was directly detected using XPS without etching. The film thickness was determined using a Dektak3 surface profile measuring system.

2.3. Cell culture

Rabbit BMSCs were obtained from the long limb bone of 28-day fetal rabbits as previously described [28], and cells in the third to the fifth passage were selected for *in vitro* experiments.

2.4. Cell adhesion and morphology

The BMSCs were seeded onto TC4, TaC and TaCN samples with a size of Φ 10 × 1.5 mm (1 × 10^4 cells per sample). After incubating for 1 and 2 h, BMSCs were fixed in 4 % paraformaldehyde, rinsed with PBS, and permeabilized with 0.1 % Triton X-100 for 30 min. The actin filaments were stained with phalloidin-FITC (Sigma, USA) conjugate solution for 50 min in the dark. Then, the cell nuclei were stained with 4′,6 diamidino-2-phenylindole (DAPI; Sigma) for 5 min. Samples were imaged using an Olympus FV1000 laser scanning confocal microscope (Olympus, USA) at 488 and 567 nm. The morphology of BMSCs was observed using SEM. After incubation for 48 h, cell samples were fixed with 2.5 % (v/v) glutaraldehyde for 2 h. Finally, the samples were dehydrated and sputtered with a thin gold film, and cell adhesion and spread were observed using the XL-30 ESEM FEG SEM (FEI Company, the Netherlands).

2.5. Cell viability and proliferation

The viability of cells in each group was evaluated after 24-h culture. Live/Dead Cell Imaging Kit (Life Technologies, USA) was used to stain the live and dead cells simultaneously. The specimens were observed using an Olympus FV1000 laser scanning confocal microscope (Olympus). For proliferation analysis, cells were seeded on TC4, TaC and TaCN samples at a density of 2 × 10^4 cells/mL and grown for 1, 4, and 7 days. On days 1, 4, and 7, the samples were transferred to new culture plates and washed twice in PBS for (5 min each). Cell Count Kit-8 (CCK-8; Dojindo, Japan) solution was added to the wells, and the samples were incubated at 37 °C for 3 h. The absorbance was measured using a Varioskan Flash Multimode reader at 450 nm (Thermo Scientific, USA).

2.6. In vitro osteogenic differentiation

BMSCs were seeded in 24-well culture plates with the DMEM and grow till they reached 60–70 % confluency. Then, the samples were incubated in the osteogenic medium (0.2 mM ascorbic acid, 10^{-8} M dexamethasone, and 10 mM β-glycerol phosphate). The medium was replaced at 3-day intervals, and cells were cultured for 4, 7, and 14 days.

2.7. Alkaline phosphatase (ALP) activity assay

ALP staining was performed on day 4 and 7 using a BCIP/NBT Alkaline Phosphatase Color Development Kit and observed under a light microscope. ALP activity was detected using an Alkaline Phosphatase Assay Kit, and OD values were measured at 405 nm. Cell lysates were used to calculate the total protein content utilizing a bicinchoninic acid protein assay kit (BCA). ALP activity was normalized to the total protein content and the reaction time. All the reagents used in this section were purchased from Beyotime Inc. (Jiangsu, China).

2.8. Calcium deposition assay

Alizarin Red S (Cyagen, China) staining was used to detect calcium deposition in BMSCs in all experimental groups after 7 and 14 days. At the designated time, BMSCs were fixed with 4 % paraformaldehyde at 4 °C for 60 min and stained with Alizarin Red S (pH 4.2) for 40 min in the dark. Then, the Alizarin Red S was removed to stop the reaction and the samples were rinsed three times with PBS (5 min each). Images of stained samples were captured using a stereoscopic microscope.

2.9. Real-time PCR analysis

RT-qPCR was performed to investigate the relative expression levels of the osteogenesis-related genes *Runx-2*, *BMP-2*, and *OPN*. After osteogenic medium treatment for 4 and 7 days, total RNA was extracted from the cells using the Animal RNAout kit (Tiandz, Inc., China), and subsequently converted into cDNA using the PrimeScript RT reagent kit with gDNA Eraser (TaKaRa, Japan) according to the manufacturer's instructions. RT-qPCR was performed using FastStart Universal SYBR Green Master (ROX) (Roche, Basel, Germany) on an Applied Biosystems 7500 Fast Real-Time PCR System (Applied Biosystems) according to the manufacturer's instructions [29]. All the results were normalized to the expression levels of GAPDH. The primers used are listed in Supplementary Table S1.

2.10. Immunofluorescence

Rat BMSCs were obtained from the long limb bone of 14-days rats, and cells in the third to the fifth passage were selected for immunofluorescence assay. Cells were seeded at a density of 50,000 cells per well in 24-well plates and processed on days 5, 7, and 15. The cells were subjected to an immunofluorescence staining protocol that includes fixation, permeabilization, and blocking with a blocking solution, interspersed with PBS washes to remove residual reagents. Primary antibodies against OPN, OCN, and RUNX2 are incubated overnight at 4 °C. Secondary antibodies conjugated with FITC are then applied at room temperature in the dark, followed by additional PBS washes. OPN (22952-1-AP) , OCN (23418-1-AP) , RUNX2 (20700-1-AP) primary antibodies and goat anti-rabbit IgG (H + L) secondary antibody (SA00003-2) was purchased from Proteintech (China).The final staining steps involve treatment with phalloidin conjugated with TRITC to label actin filaments and DAPI to stain the nuclei. Visualization is carried out using a confocal laser scanning microscope (OLYMPUS FV3000). The quantitative analysis of the immunofluorescence staining were measured by the Image J. A thresholding strategy was employed to measure the areas of both the cell nucleus and the expressed proteins. The ratio of the fluorescent area of the expressed proteins to the area of the cell nucleus was calculated, achieving normalization of fluorescence intensity.

2.11. In vivo experiments

All animal procedures were approved by the ethics committee for Jilin University and carried out according to the guidelines followed in China. Before surgery, a total of 24 male Japanese White Rabbits (2.5−3.0 kg) were housed in the animal laboratory for 7 days towards acclimatization. Then, all animals were randomly divided into three groups. After the rabbits were anesthetized via pentobarbital sodium and Antai injection (DMK Biological Technology Co., China), both hind legs were shaved and disinfected with povidone-iodine solution. Subsequently, the femur was exposed via skin incision, and a hole was drilled into the distal surface of each femur. Finally, two screws with different surface properties were randomly implanted into the two holes (Supplementary Fig. S1) (8 screws in each group). Next, the incision was carefully sutured and animals were injected with gentamicin for 3 days to prevent infection. All rabbits were sacrificed using excessive anesthetics 12 weeks after surgery, and all femur samples with screw implants were harvested and fixed with 4 % paraformaldehyde.

2.12. Micro-CT evaluation

The femur samples were scanned using Micro-CT (quantumGX; PerkinElmer, USA) to evaluate the newly formed bone around different samples. The parameters of scanning were 90 Kv and 88 Ua at a resolution of 36 μm. After scanning, 2D images were directly exported for observation. 3D models were reconstructed using the 3D Viewer software provided with the equipment. The bone volume/total volume (BV/TV) and fraction of the tissue around the screws in the region of interest were analyzed to evaluate the osseointegration ability.

2.13. Histomorphometric and histological observation

After fixation in 4 % paraformaldehyde, the femur samples containing implants were dehydrated in a graded series of ethanol (from 75 % to 100 %), and subsequently embedded in methyl methacrylate resin. Next, the specimens were cut into 200–300-μm-thick sections perpendicular to the long axis of the femoral shaft using a Leica SP1600 saw microtome (Leica, Germany). The sections were subsequently ground and polished to a final thickness of about 50 μm and stained using 1.2 % trinitrophenol and 1 % acid fuchsin (Van Gieson staining). The histological images were obtained using an Olympus IX71 microscope (Olympus), and the newly formed bone areas were analyzed via ImageJ 1.50i software.

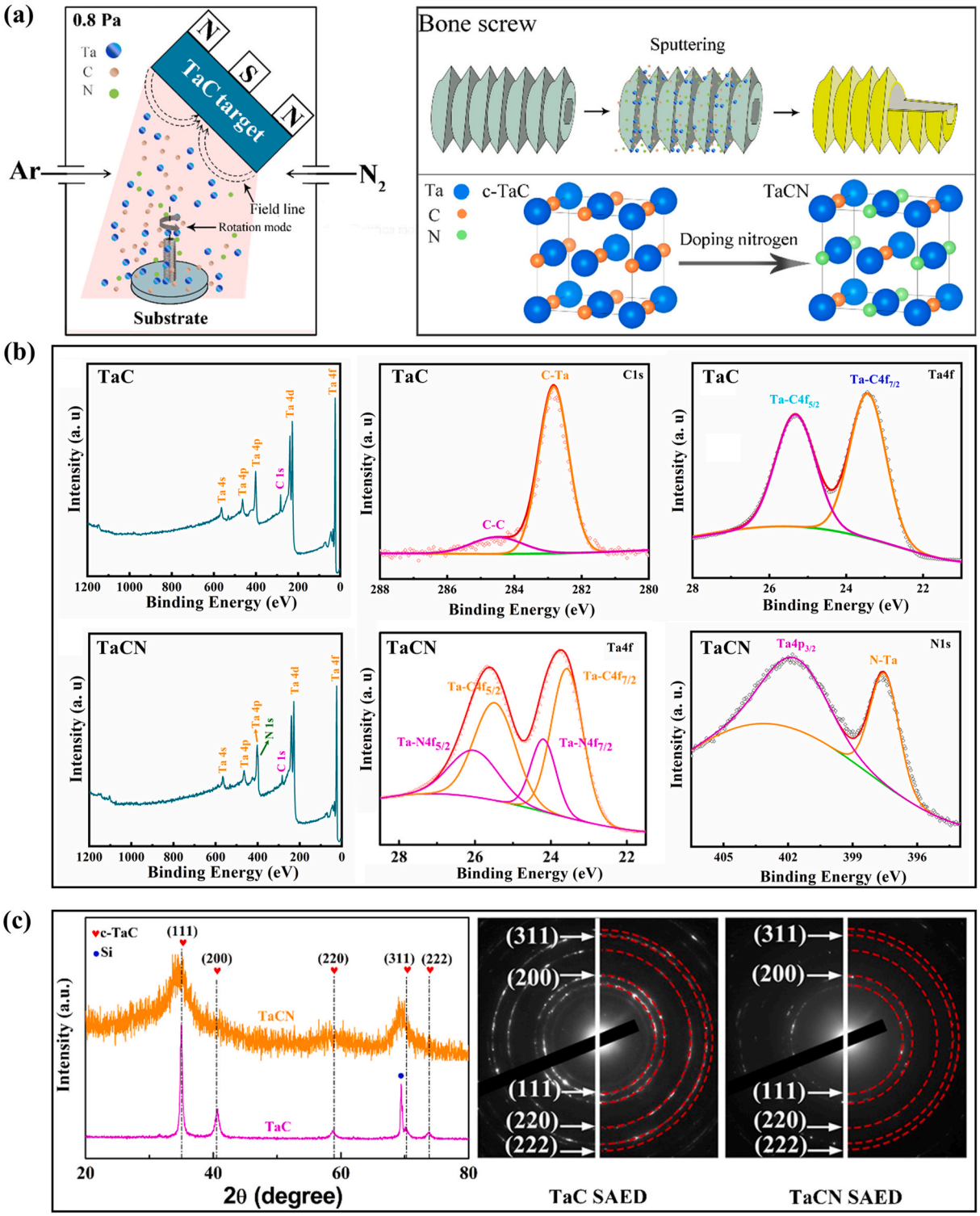

Fig. 1. (a) Schematic representation of the growth process using TaC and TaCN films on bone screw during magnetron sputtering, and the crystal structure of TaC and solid TaCN. (b) Ta4f and C 1*s* core-level spectra for TaC, and Ta4f and N 1*s* core-level spectra for TaCN. (c) XRD and SAED patterns for the films.

2.14. Quantification of protein adsorption

Histone (H9250, Sigma Aldrich) and bovine serum albumin (Sigma Aldrich) were selected as representatives of positively and negatively charged proteins. A total of 2 mL of protein solution (0.25 mg/mL) was applied on the samples (4 cm^2), which were incubated at 37 °C for 60 min and washed with 5 mL PBS three times to remove unbound protein. Finally, samples were air-dried and analyzed using BCA protein assay kit as per the standard procedure. All experiments were performed three times, in duplicate.

2.15. Protein array

All animal procedures were approved by the ethics committee for Jilin University and carried out according to the guidelines followed in China. SD rats (male, 8 weeks old, Changsheng biotechnology co., Ltd., Liaoning, China) were randomly divided into TaC and TaCN groups. Specimen were implanted into the subcutaneous pockets of SD rats. The animals were anesthetized with Antai injection (DMK Biological Technology Co.). To implant the scaffolds, 20-mm incisions were made on each dorsal side. Each specimen was then placed into the subcutaneous pocket. To measure protein adsorption, we first inserted the scaffolds into cages, which were subsequently implanted into the subcutaneous tissue. The cytokines and GFs accumulated on the TaC and TaCN samples were analyzed 48 h post-implantation. Lysates obtained from the specimens were quantified using a protein array kit (RayBiotech, USA) and the same amount of protein lysate was loaded on the array membrane, following the manufacturer's instructions. The results of the protein array were visualized and quantified using ImageQuant LAS4000 Scanner (GE Healthcare).

2.16. Statistical analysis

Student's *t*-test was used to determine significant differences in the mean values of the proliferation rate, ALP activity, gene expression, and bone volume between groups. Results with $P < 0.05$ were considered statistically significant. All results are presented as the mean ± SD. GraphPad Prism 8.02 software was used for all statistical analyses.

3. Results and discussion

3.1. Deposition and characterization of the films

The growth of films during sputtering mainly included an intermixture of atoms in the plasma, diffusion, and grain growth of thermally activated atoms on the rotating substrate surface. TaC films were deposited on Si (100), TC4 substrates and bone screws by TaC composite target using reactive magnetron sputtering in the presence of Ar, and TaC films doped with N were grown in the presence of Ar and N_2 [see *Methods* for more details], as illustrated in Fig. 1a.

Based on the relative intensities of the Ta 4*f*, C 1*s*, and N 1*s* XPS peaks as shown in Fig. 1b, we quantified the elemental composition of the coatings. For coatings deposited in pure Ar ($F_{N2} = 0$ sccm), the analysis yielded a composition of $TaC_{0.92}$. In contrast, whereas for depositions with $F_{N2} = 30$ sccm, the emergence of the N 1*s* peak led to an asymmetric Ta 4p peak, and a marked reduction in the relative intensity of the C 1*s* peak. The resulting composition for this condition was $TaC_{0.49}N_{0.5}$. The chemical bonding status of the as-deposited films was also investigated using XPS, as shown in Fig. 1b. In the XPS core-level spectra of Ta4f and C 1*s* for the pure TaC film, two distinct peaks at binding energies of 23.4 eV and 25.3 eV were found for Ta4f, which can be attributed to the Ta-C bonds [30]. Furthermore, the typical XPS spectra of C 1*s* exhibited two deconvoluted peaks at 282.7 eV, which are related to C bonded to Ta [31], and another slight peak at 285.0 eV as a result of the sp^2-hybridized bonding of C in an amorphous phase [32,33]. For the XPS core-level spectra of Ta4f, C 1*s*, and N 1*s* of the TaCN film, the Ta4f spectrum exhibited two similar peaks to the TaC film. These two broader peaks could be deconvoluted into two well-separated doublets. The lower energy peak of doublet for Ta $4f_{7/2}$ was around 24.3 eV, indicating that some Ta-N bonds were also formed in addition to the Ta-C bonds [34]. In the XPS spectra of C 1*s* for the TaCN film, all peaks were the same as that of TaC (not shown); no C-N peak at 287.2 eV was observed [35,36], indicating that no C-N bonds formed in the films. To further confirm this result, we measured the XPS N 1*s* spectra and found that the peak at 397.2 eV corresponded to the N-Ta bond [37]; no N-C bonds were detected, confirming that all N atoms were bonded to Ta. Based on the XPS results, we concluded that both C and N atoms were bonded to Ta atoms on the TaCN film, co-occupying the interstitial sites of the Ta sublattice; no C-N bonds were formed. However, it was difficult to clarify the phase structure of TaCN films, because they either existed in the TaCN solid solution structure or the TaC + TaN mixed structure. Therefore, X-ray diffraction (XRD) experiments were carried out for each sample (Fig. 1c). For the TaC film, five diffraction peaks were assigned to (111), (200), and (220) reflections of the centered cubic B1-NaCl structure (JCPDF: 35–0801). For the TaCN film, all the peaks belonged to the B1-NaCl TaC structure, no new peaks corresponding to TaN were observed, indicating N atoms formed a solid solution structure rather than TaN phase. In addition, all peaks were weaker and broader than their counterparts in the TaC film, which was attributed to a lower crystalline quality. The selected area electron diffraction (SAED) patterns for TaC and TaCN (Fig. 1c) further confirmed the formation of the NaCl solid structure instead of the TaC_x + TaN_y mixed structure. According to the above analyses of XPS, XRD, and SAED, the C sublattice vacancies were occupied by the added N to form the TaCN solid structure. The cross-section morphology and the corresponding EDS analysis for Ta, C, and N elements for the TaC and TaCN samples are shown in Fig. 2. All samples exhibited smooth surfaces without noticeable growth defects. Further magnification (Fig. 2a) revealed that the microsurface morphologies of the two types of samples were essentially identical, and the addition of nitrogen did not cause significant changes to the surface of the TaCN film. The energy dispersive x-ray spectrometry (EDS) mapping results revealed that nitrogen was incorporated successfully in the coating and distributed homogeneously. Further characterization cross-section morphology and corresponding elemental mapping of the films are shown in Fig. 2b. The thicknesses of the TaC and TaCN films are approximately 1.34 μm and 1.44 μm, respectively, while the Ta layer is about 0.16 μm thick. The interface between the films and the titanium alloy substrate demonstrates excellent adherence, with no signs of delamination or compromise in structural integrity.

3.2. Cell spreading and morphology

To understand the influence of the films on initial cell spreading and morphology, we performed F-Actin and nuclei staining on BMSCs after 1- and 2-h cultures. After 1 h (Fig. S2), the cells in all groups shrunk slightly; however, cell adhesion improved after 2 h (Fig. 3a). Among the TC4 groups, the cells shrunk slightly and exhibited variable sizes. In contrast, cells in the TaC and TaCN groups showed a diffuse cytoskeleton with clearer microfilaments and microtubules in the cytoplasm. These results demonstrated that TaC and TaCN films enhanced initial cell spreading. To observe long-term cell adhesion and morphology, the cells in different groups were imaged using SEM after a 48-h culture (Fig. 3b–d). Extensive cell spreading was observed in the TC4 group (Fig. 3b), but cells were shrunken and isolated; moreover, it was hard to observe pseudopodia in higher magnification images. In the TaC group (Fig. 3c), the cells on the sample surface were fully spread, showed a polygonal morphology, and established cell-to-cell contact. However, few pseudopodia were observed at higher magnification. As shown in Fig. 3d, the cells on the TaCN surface showed a similar morphology to those grown on TaC and exhibited cell-cell interactions. Moreover, there were more pseudopodia in cells grown on TaCN than in cells from the other two groups. The improved cell interaction and extension of

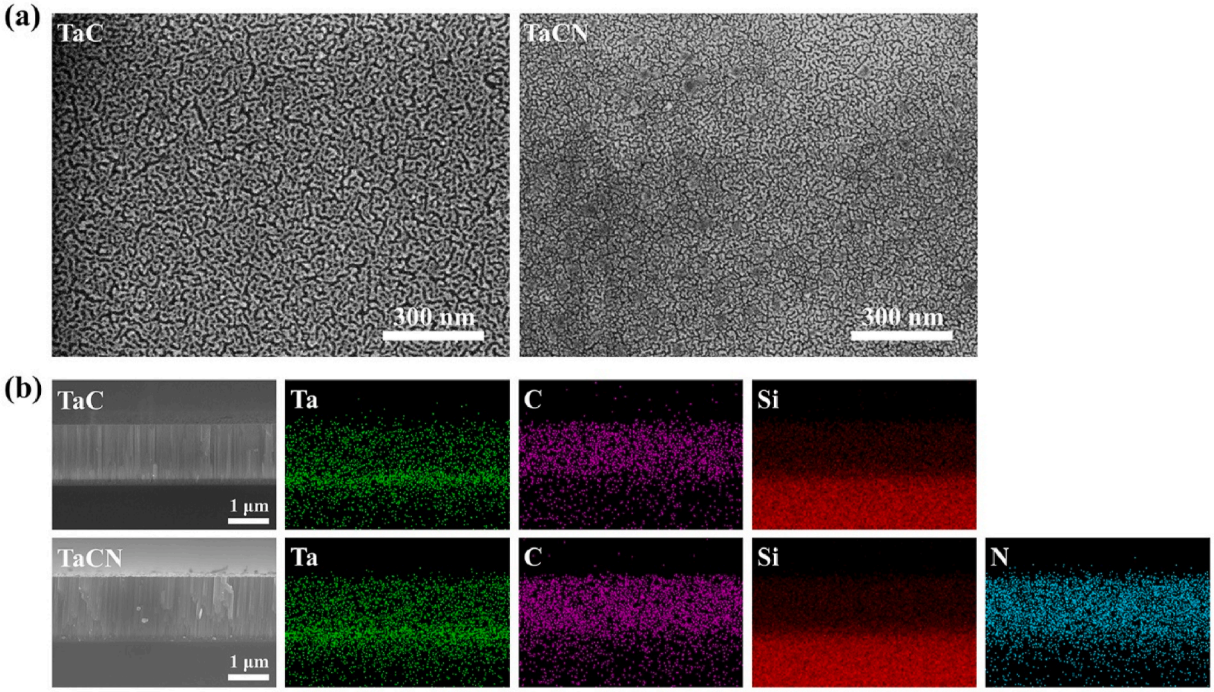

Fig. 2. (a) SEM images of surface morphology for TaC and TaCN samples. (b) SEM images of the cross-section morphology and corresponding EDS analysis for Ta, C and N elements for TaC and TaCN samples.

pseudopodia in the TaCN group indicated that cell attachment and spreading was better compared to those in the TC4 and TaC groups, and was consistent with F-Actin and nuclei staining results. Thus, the TaC and TaCN groups are speculated to be more favorable for cell spreading than TC4, making them better platform for recruiting BMSCs to the site of the bone defect. Additionally, the nuclear adhesion on the surface of different samples (Fig. S3) confirmed that the TaC and TaCN groups recruited more cells than the TC4 group.

3.3. Cell viability and proliferation

To measure the influence of different films on cell viability, we seeded BMSCs on plates and allowed them to grow for 24 h. The fluorescent images obtained using the live/dead cells kit showing cells on different surfaces are illustrated in Fig. 3e. All groups had many live cells and few dead cells, but more dead cells were observed in TC4 group compared with those in the TaC and TaCN groups, suggesting the non-cytotoxic nature of TaC and TaCN films. The relative rate of cell death expressed as a percentage (Fig. S4) also indicated that TaC and TaCN films had high cytocompatibility. Next, the proliferation of BMSCs on different films was analyzed as shown in Fig. 3f. On the first day, the number of cells was similar in both the TaC and TaCN groups, and was slightly higher than that in the TC4 groups. On day 4, cell proliferation increased in all groups, and was significantly higher in the TaC and TaCN groups than in the TC4 groups. On day 7, the growth rates for cells in TC4 and TaC groups slowed down gradually, finally reaching a plateau. However, the cell growth rate was significantly higher for TaCN groups than for the other groups ($P < 0.05$), which suggested that TaCN was the best surface for cell proliferation. Moreover, TaCN film showed the highest cell adhesion and proliferation among all experimental groups, which would facilitate the subsequent osteogenic differentiation.

3.4. Evaluation of osteogenic activity in vitro

An ideal bone biomaterial should have the ability to promote cell osteogenic differentiation [38]. To investigate cell differentiation, ALP-positive areas of each sample were stained after 4 and 7 days, as shown in Fig. 4a. On day 4 of culture, the ALP-stained areas were comparable in each group. On day 7, the percentage of ALP-stained areas increased in all the groups, but the increase was highest in the TaCN group. Fig. 4b shows the quantification of ALP activity. ALP activity increased in all the groups from day 4–7. On day 4, no significant differences were observed in any of the groups. On day 7, ALP activity was significantly higher in the TaCN group than in the other groups. To further understand the cellular mechanism behind the improved osteogenic differentiation on the TaCN film, we quantified the relative expression levels of osteogenic genes such as *BMP-2*, *Runx-2*, and *OPN* via quantitative real-time PCR (RT-qPCR), as shown in Fig. 4c. After 7 days of osteogenic treatment, all genes showed a significantly higher expression in the TaCN group compared to that in the TC4 group. On the contrary, in the TaC group, although the expression levels of *BMP-2* and *Runx-2* were higher than those in the TC4 group, the expression of *OPN* was similar to that of the TC4 group. The immunofluorescence staining and quantitative analysis of OCN, OPN and Runx-2 are shown in Fig. 5a and b. The OCN expression in TaCN group was significantly higher than that in other groups on day 5 and 7 ($p < 0.05$). On day 5, the OCN expression in the TaC group was higher than that in the TC4 group ($p < 0.05$). While there was no significant difference in the OCN expression between TaC group and TC4 group on day 7 and 15. Regarding OPN expression, the TaCN group had the highest OPN expression among the three groups on day 5, 7, and 15($p < 0.05$). On days 5 and 7, the OPN expression level in the TaC group was similar to that in the TC4 group. On day 15, the OPN expression in the TaC group was higher than that in the TC4 group ($p < 0.05$). Regarding Runx-2 expression, on day 5, 7, and 15, the expression in the three groups, from highest to lowest, were TaCN, TaC, and TC4. From day 5 to day 15, the Runx-2 expression in TaC and TaCN group was significantly higher than that in TC4 group($p < 0.05$). Collectively, these results suggested that TaCN film was superior to TaC in inducing BMSCs differentiation.

3.5. Evaluation of bone healing efficacy in vivo

Micro-CT analysis was used to evaluate the new bone formation and

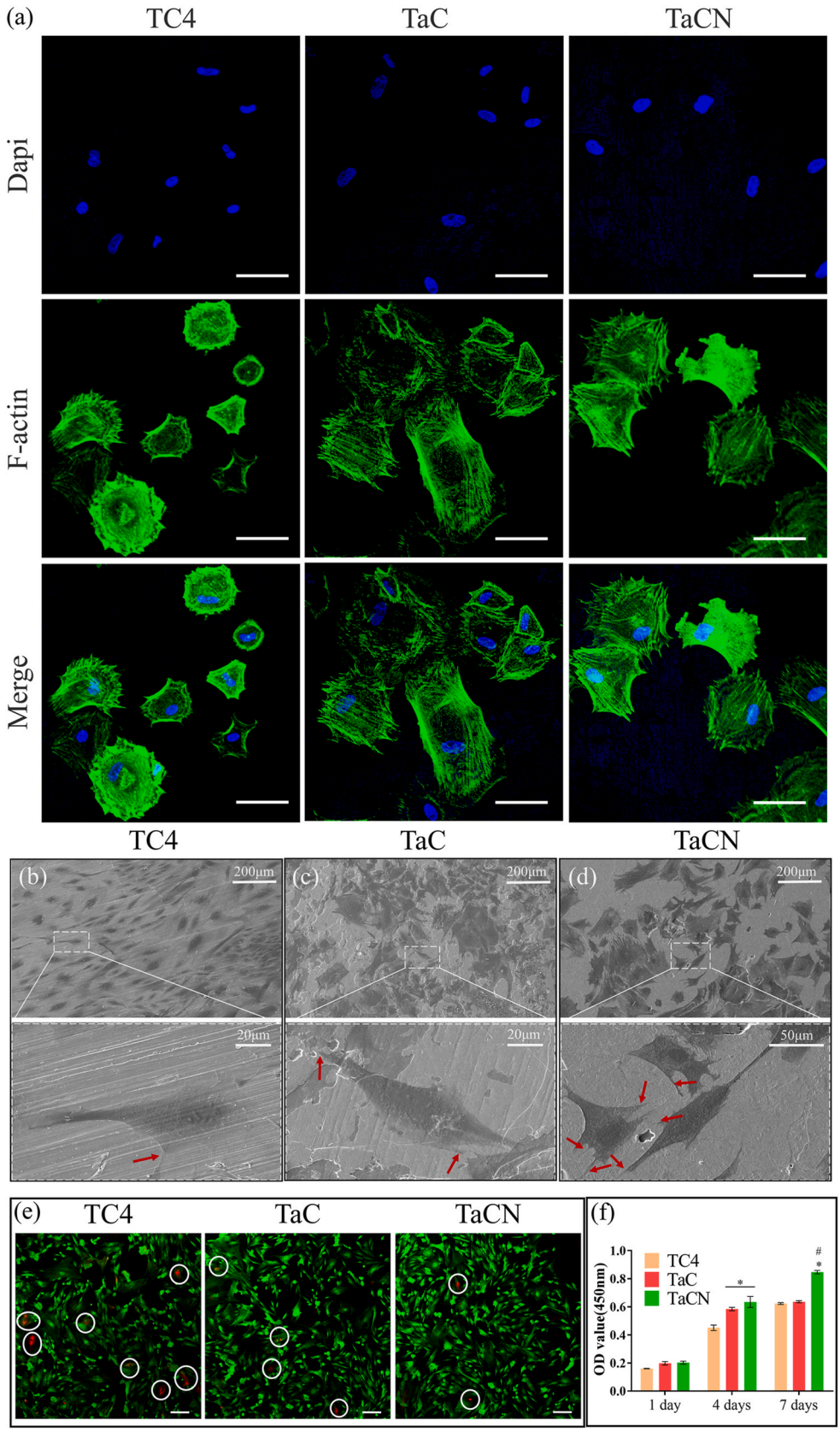

Fig. 3. (a) F-Actin and nuclei fluorescence staining of BMSCs after 2 h of culture on different surfaces. The nuclei are shown in blue, F-Actin in green. Scale: 50 μm. (b–d) Scanning electron microscopy images of BMSCs cultured on (b) TC4, (c) TaC, and (d) TaCN for 48 h. (e) Fluorescence images showing live/dead staining of BMSCs cultured on TC4, TaC, and TaCN for 24 h. Live cells are shown in green, and dead cells are in red. Scale: 100 μm. (f) The proliferation of BMSCs on different films evaluated via the Cell Counting Kit-8 assay after 1, 4, and 7 days of culture. $^{*}P < 0.05$ vs TC4; $\#P < 0.05$ vs TaC. (For interpretation of the references to color in this figure legend, the reader is referred to the Web version of this article.)

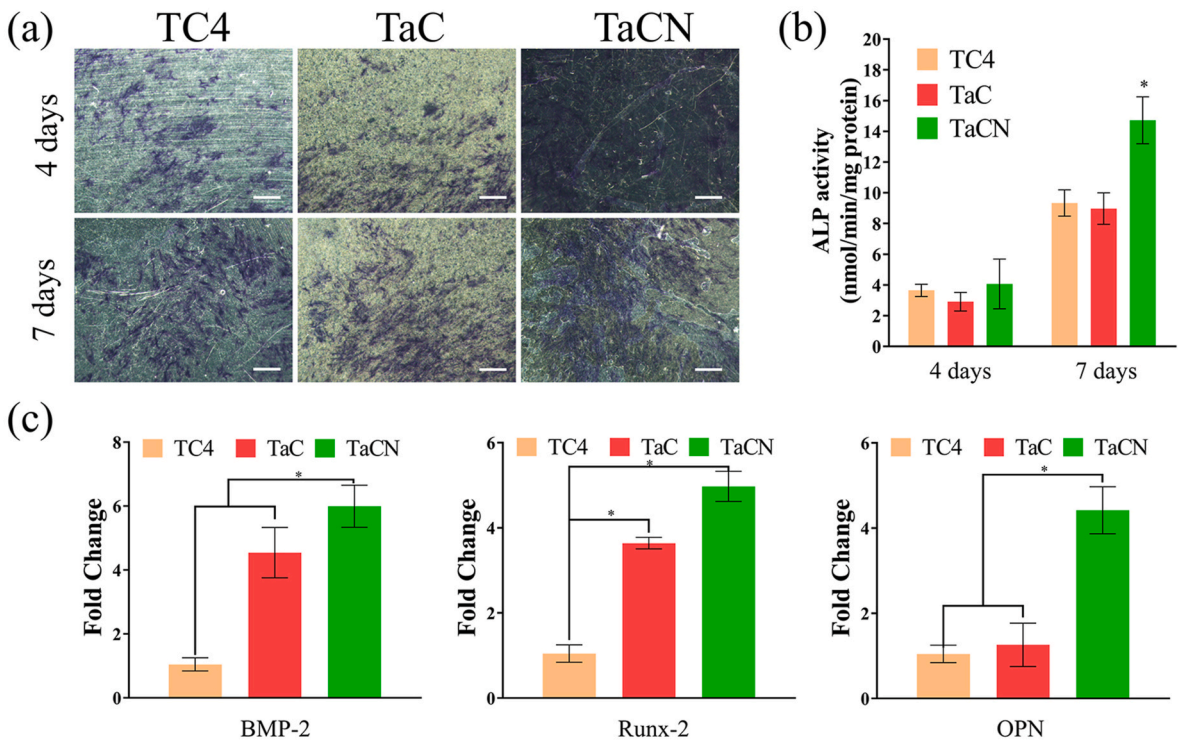

Fig. 4. (a) Alkaline phosphatase (ALP) staining showing the percentage of ALP-stained areas in each group 4 and 7 days after osteogenic medium treatment. (b) Quantification of ALP activity for all groups 4 and 7 days after osteogenic medium treatment. *$P < 0.05$ vs other groups. Scale: 100 μm. (c) Relative expression levels of BMP-2, Runx-2, and OPN after 7 days of osteogenic treatment. *$P < 0.05$.

osseointegration around different films 12 weeks after implantation. Representative 2D cross-sectional images and the 3D reconstructions are shown in Fig. 6a, and the bone tissue was marked with green in the software images. When 2D and 3D images were combined, we observed that the newly formed bone tissues were distributed circumferentially around the implant in all groups, and the belt of the regenerated bone around the TaCN screw was wider than that of the other groups. In addition, the bone volume/total volume (BV/TV) fraction was used to evaluate the relative bone formation and osseointegration. As shown in Fig. 6b, the BV/TV fraction for TaCN and TaC groups was significantly higher than that for the TC4 group, and TaCN showed the highest value. These results suggested that both TaC and TaCN films improved bone regeneration in the animal model, and that TaCN was superior to the other two films.

The integration status of the new bone around different implants was observed via Van Gieson staining. Fig. 6c shows the bone histology around different implants after 4 and 12 weeks. At 4 weeks after the implantation, the new bone around all the implants was loosely structured, whereas the condition of the bone in the TaC and TaCN groups was better than that in the TC4 group; new bone formation was established around the implant in all groups. With bone remodeling, we expected the new bone tissues to become dense and tightly attached around the implant by 12 weeks after implantation. Our results showed that the TC4 group had the greatest areas of the implant covered by a thick layer of fibrous tissue, and the bone was separated from the implant surface. Fibrous tissues also emerged on the surface of the TaC implant, but the thickness and amount were less than those in the TC4 group. In contrast, the new bone of the TaCN group showed excellent osseointegration, in which most areas of the bone tissue around the implant were in direct contact with the TaCN surface.

3.6. Analysis of the changes in chemical bonding and surface charge in body fluid

The biological behavior of cells is highly regulated by the surface topography properties, such as roughness, wettability, and local chemical microenvironment [39,40]. In the present study, we first eliminated the contribution of roughness and wettability on cell adhesion (Figs. S5 and S6). In bone regeneration, the suitable local environment (as indicated by the micro-nano structures and morphology), nucleation of extracellular minerals, and biomolecular signals (provided by GFs) play important roles. Therefore, we analyzed the changes in the local environment in the body fluid. The surface chemical status of the TaC and TaCN films was examined using XPS after soaking them in simulated body fluid (SBF) for 72 h, as displayed in Fig. 7. We observed that Ta4f peaks for the TaC film (Fig. 7a) could be fitted with four $4f_{7/2}/4f_{5/2}$ spin-orbit doublets, along with 1.9-eV intervals in binding energies (BE). The doublets at 27.6/25.7 eV were assigned to the Ta oxidation state [41], and the other two peaks at lower BE belonged to the Ta-C bond. Corresponding peaks at 282.9, 284.4, 286.0, and 287.9 eV in C 1*s* spectra (Fig. 7b) were ascribed to C-Ta, C-C, C-O, and C=O, respectively [22,42–44]. This process was elaborated using the following oxidation reaction:

$$\text{Ta-C} + O_2 \rightarrow TaO_xC_y \quad (1)$$

Self-oxidation was observed in the case of the TaCN film. As shown in Fig. 7c (Ta4f spectrum), in addition to the Ta-C and Ta-N bond, the doublets at 27.7 and 25.8 eV corresponded to the chemical state of TaO_xN_y [45]. Meanwhile, C-Ta, C-C, C-O, and C=O bonds were also identified in the C 1*s* spectrum of TaCN (not shown). In the N 1*s* spectrum (Fig. 7d), the strong peak around 399.7 eV could be attributed to the amino groups and N-O bond [46,47]. In particular, on the partially oxidized TiN surface, water molecules are adsorbed in a dissociative manner because the partially oxidized TiN has a mixed-valence character. The charge transfer from titanium to the adsorbed oxygen atoms

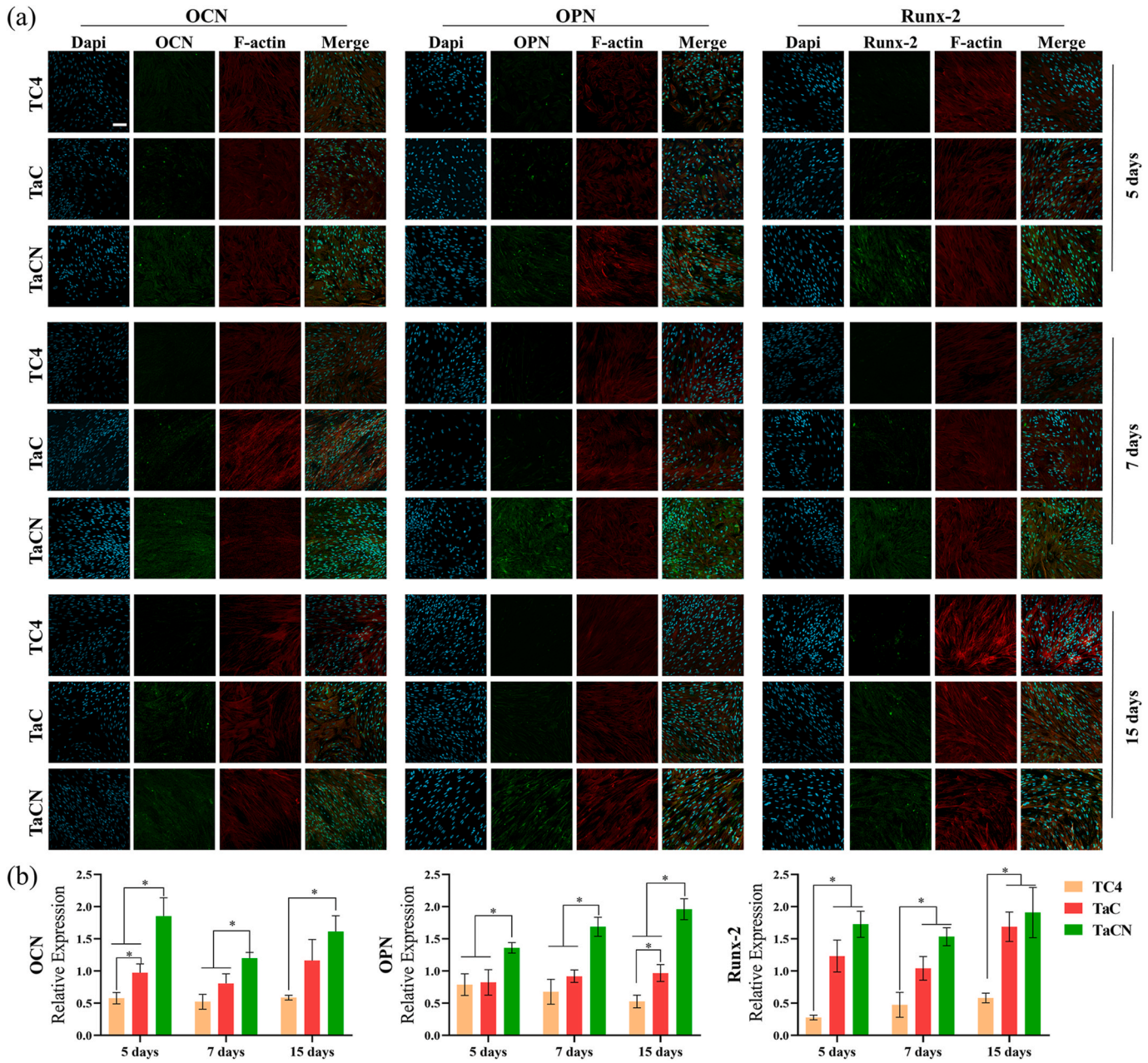

Fig. 5. (a) The representative immunofluorescence staining of OCN, OPN and Runx-2 for all groups 5, 7 and 15 days after osteogenic medium treatment. Scale: 100 μm (b) The quantitative analysis of the immunofluorescence staining. $^{*}P < 0.05$.

leads to the depletion of electrons in the *d* orbitals of titanium atoms, which localizes the negative charge on the bridging oxygens [48]; this model also makes sense for the partially oxidized Ta-N surface. Based on the above analysis, in addition to reaction (1), oxidation and hydration of the partially oxidized TaCN surface might occur as follows [27]:

$$Ta - N + O_2 \rightarrow TaO_xN_y \quad (2)$$

$$Ta - N + H_2O \rightarrow TaO_xN_y + NH_4^+ + OH^- \quad (3)$$

Compared with the self-oxidation reaction on the TaC surface, the TaCN film soaked in SBF could absorb O_2 and H_2O, yielding TaO_xN_y, ammonium (NH_4^+), and hydroxide ions (OH^-). To clarify the occurrence of reaction (3), we soaked TaC and TaCN films for 72 h in the SBF solution and measured the pH variation (Fig. S7). The pH for the TaC film slightly increased from 7.40 to 7.49, while that of the TaCN film increased from 7.40 to 7.72; these observations further validated occurrence of reaction (3). This change in pH might be due to the field force behavior induced by N incorporation on the surface, where different atoms possess different electron and vacant states. Doped N changed the energy and force interactions, which resulted in the different oxidation products between TaC and TaCN. We expected the negative charges localized on the bridging oxygen atoms of the partially oxidized TaCN surface to play an important role in enhancing the bioactivity of TaCN, since the electrostatic interaction between the Ca or P ions and the negatively charged surface are important factors to induce Ca-P nucleation [49,50]. In addition, the electrical resistivity of TC4, TaC, and TaCN was 1.78×10^2 [51], 42.1 [52], and 6.0×10^3 μΩ cm [53], respectively. TaCN coating exhibited the lowest conductivity, which would prolong the survival of ions produced during the surface reaction and assist *in vitro* osteogenic differentiation and *in vivo* osseointegration. Lower conductivity of the partially oxidized and hydrated TaCN surface enables the spontaneous nucleation of calcium

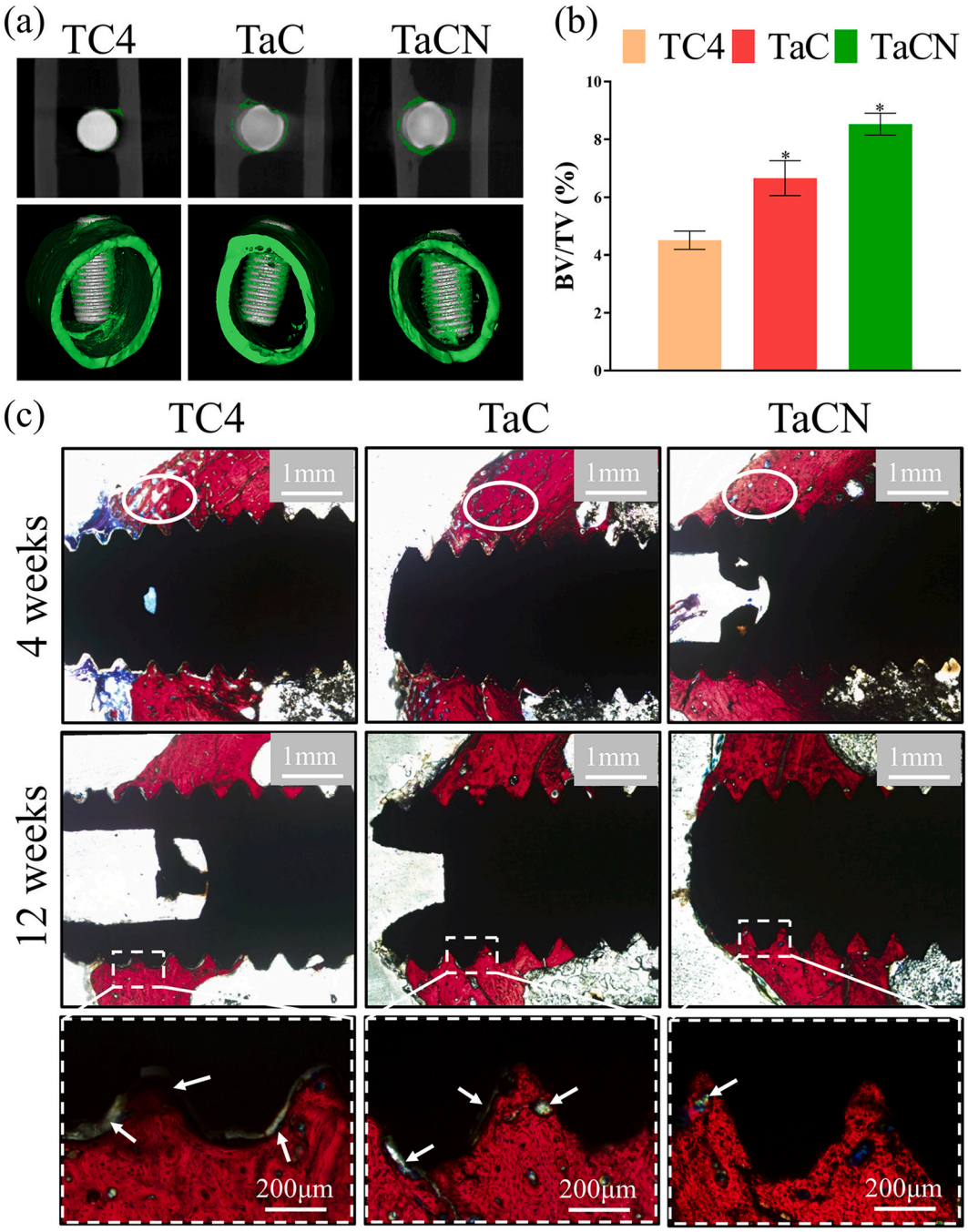

Fig. 6. (a) Representative cross-sectional Micro-CT 2D images and 3D representations of different groups after 12 weeks. The bone tissue was marked with green on the images. (b) Quantitative analysis of the bone tissue in the region of interest using Micro-CT. *$P < 0.05$ vs TC4. (c) Histological images of bone around the implants using Van Gieson staining at 4 and 12 weeks. The bone tissue is stained in red. Fibrous tissue is stained in yellow. The implant is indicated in black. The white arrows indicate the fibrous tissue and gap. (For interpretation of the references to color in this figure legend, the reader is referred to the Web version of this article.)

phosphate without requiring any previous deprotonation [48]. When the TaCN coating was soaked in osteogenic induction medium, the local supersaturation degree exceeded the critical level necessary for apatite nucleation due to the presence of excess Ca^{2+}, HPO_4^{2-}, and OH^- ions. Thus, calcium phosphate content can be increased by consuming Ca^{2+} and HPO_4^{2-} according to the following equilibrium [54]:

$$10Ca^{2+} + 6HPO_4^{2-} + 8OH^- \rightarrow Ca_{10}(PO_4)_6(OH)_2 + 6H_2O \quad (4)$$

As discussed above, the hydrolysis reaction (3) on the TaCN surface is the key factor to enhance its bioactivity relative to the TaC coating, while consuming protons and raising the OH^- concentration contribute to the negatively charged surface and the increase the ionic activity to accelerate the rate of apatite formation [54,55]. Fig. S8 showed the XRD patterns of samples after 7 days of immersion in Simulated Body Fluid (SBF). Apart from the substrate peaks, the XRD curves of the TaC and TaCN samples exhibited peaks corresponding to hydroxyapatite (PDF#74–0565). Additionally, peaks matching CaP (PDF#16–0728) and Ca3P2 (PDF#16–0730) were also observed. This indicated that the TaC and TaCN samples were capable of inducing mineralization in a simulated body fluid environment. After osteogenic medium treatment for 7 and 14 days, calcium deposition was assayed using Alizarin Red staining for calcium nodules. Furthermore, the calcium nodule

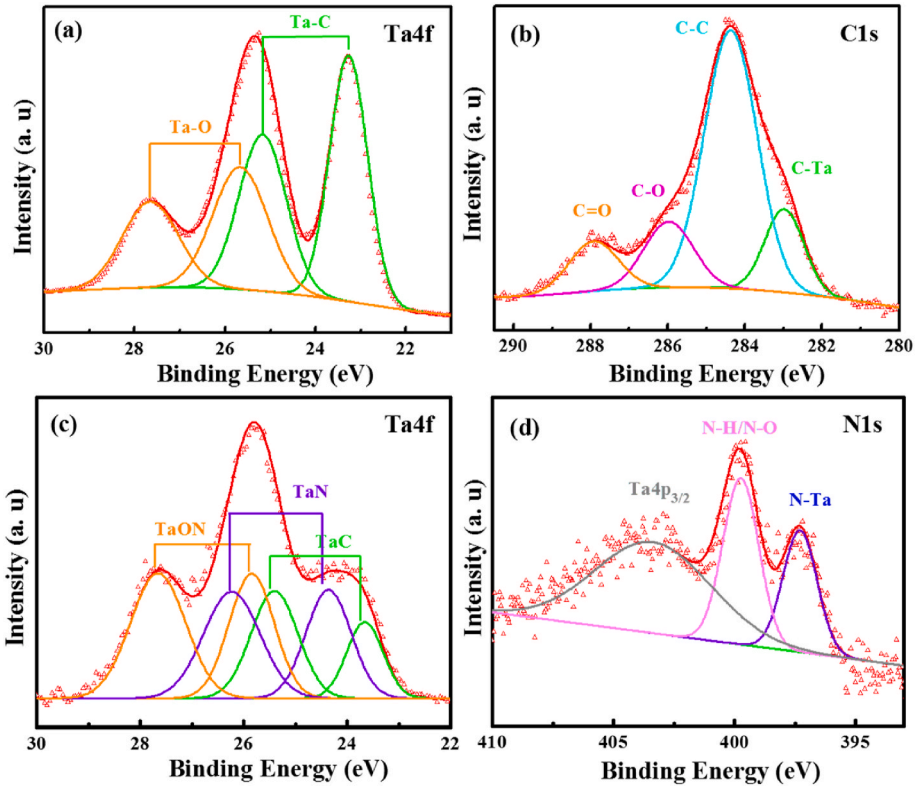

Fig. 7. (a) Ta4f, (b) C 1*s* core-level spectra for TaC films, and (c) Ta4f, (d) N 1*s* core-level spectra for TaCN films. All *in vitro* treated samples were immersed in simulated body fluid for 72 h.

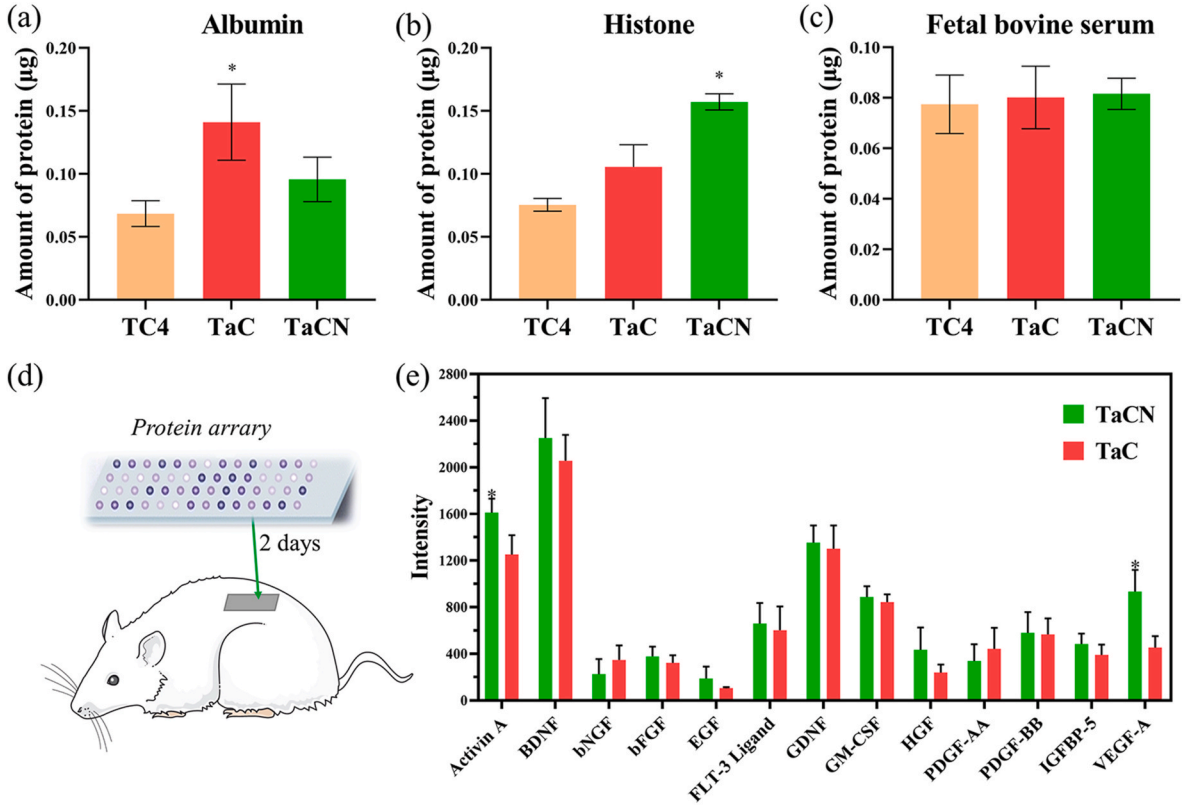

Fig. 8. The recruitment ability of TaC and TaCN for albumin(a), histone(b) and fetal bovine serum(c). Histone and albumin were selected as typical representatives of positively and negatively charged proteins, and fetal bovine serum was selected as a mixture of multiple proteins. (d) Protein array analysis of growth factors adsorbed to scaffolds after 2 days. (e) The intensity of representative growth factors adsorbed to TaC and TaCN films. $^{*}P < 0.05$.

deposition after osteogenic induction treatment was examined using Alizarin red staining. It can be seen that the TaCN group has more red-stained calcium nodules, indicating that, compared to the TC4 and TaC films, the TaCN film promotes the mineralization of extracellular matrix (Fig. S9).

3.7. Evaluation of the recruitment of proteins and cytokines in vitro and in vivo

To demonstrate the adsorption effect of the TaCN coating on positively charged proteins, serum albumin (negatively charged) and histone (positively charged) were selected as representative proteins for the experiment. As shown in Fig. 8a, the amount of serum albumin adsorbed on TaCN is significantly lower than that on the TaC group (the difference was significant, $P < 0.05$), indicating that the surface of TaCN repels negatively charged proteins. Furthermore, in the histone adsorption experiment(Fig. 8b), TaCN exhibited a significantly higher adsorption capacity compared to the other groups (the difference was significant, $P < 0.05$), proving its pronounced adsorption effect on positively charged proteins. These results indicate that TaCN can adsorb positively charged proteins, suggesting that positively charged growth factors could also be adsorbed on the surface of TaCN. Additionally, fetal bovine serum was used to represent mixed proteins in evaluating the adsorption effects on proteins of different samples in a mixed-protein solution(Fig. 8c). The results showed that the total amount of mixed protein adsorbed by the three groups was similar, indicating that in the presence of both positively and negatively charged proteins, the protein adsorption capacity of the TaC and TaCN groups was not superior to that of the TC4 group. This also suggests that the morphological changes of the coatings are not the reason for the differences in protein adsorption amounts.

Commonly used BGFs in bone tissue engineering include bone morphogenetic proteins (BMPs), insulin-like factors (IGFs), TGFβs, fibroblast GFs (FGF) and vascular endothelial GFs (VEGFs). In addition, the isoelectric point of most BGFs is higher than pH 8.0, and they are positively charged in the body fluid (pH 7.35–7.45) [56–58]. Based on the results of the *in vitro* protein adhesion experiments, it can be inferred that the TaCN coating may recruit the positively charged BGFs. Therefore, subcutaneous implantation experiments in rats were used to further evaluate the adsorption effects on proteins and cytokines in bodily fluid environment, and the adsorption amounts of various proteins was analyzed using protein array experiments(Fig. 8d and e). The results showed that most positively charged proteins and cytokines were more easily adsorbed by TaCN, with higher adsorption amounts than the TaC group; however, except for the proteins Activin A(members of a family of TGFβs) and VEGF-A, the differences in the other proteins were not statistically significant. This may be attributed to the variety of positively charged proteins and cytokines in the bodily fluid, which compete with each other during adsorption by TaCN, thereby diminishing the differences in the adsorption amounts of individual proteins or cytokines. Nonetheless, the results indicate that TaCN tends to adsorb positively charged growth factors such as Activin A, VEGF-A, bFGF, which are crucial in osteogenic differentiation and angiogenesis. Both *in vitro* and *in vivo* results suggested that positive BGFs would be recruited on the surface of implants, and contribute to *in vivo* osseointegration.

4. Conclusion

In this study, we report a novel strategy to regulate the chemical bond status of different films to construct an osteoinductive surface that would facilitate bone regeneration via recruitment of host BGFs. TaC and TaCN films were prepared via magnetron sputtering, and the biocompatibility and osteogenesis for both coatings were examined. For comparison, the TC4 alloy was used for the same measurements. Biocompatibility analysis suggests that both TaC and TaCN enhanced cell adhesion and proliferation. Moreover, osteogenesis experiments confirmed that the TaCN film enhances osteogenic differentiation *in vitro* and improves bone healing *in vivo*. Through further characterization of the surface chemical bond status and protein array analysis, we provide evidence that TaCN exhibits a negatively charged surface with abundant functional groups (OH^-), and the positively charged host BGFs are enriched on the surface of implants to improve bone healing. Under the forementioned cascade effect, TaCN shows superior performance of osseointegration *in vivo*, in which the amount of newly formed bone around the TaCN implant is nearly 2-folds higher than that around the Ti6Al4V implant, and the bone tissues around the implant are in direct contact with the TaCN surface. The excellent osseointegration of TaCN film demonstrates that it can be a potential method to enhance osseointegration for artificial bone tissue engineering. More importantly, this work provides an innovative and clinically transformable strategy to improve bone healing via mobilizing host BGFs to the site of repair.

CRediT authorship contribution statement

Ruiyan Li: Writing – original draft, Methodology, Investigation, Conceptualization. **Kan Zhang:** Writing – review & editing, Methodology, Conceptualization. **Chuanyao Dong:** Validation, Investigation. **Kaiwen Wang:** Validation, Investigation. **Xinlei Gu:** Validation, Software, Investigation. **Yanguo Qin:** Writing – review & editing, Project administration, Methodology, Conceptualization.

Declaration of competing interest

The authors declare no competing financial interest.

Data availability

Data will be made available on request.

Acknowledgments

The support from National Natural Science Foundation of China (Grant Nos. 52322206, U21A20390), Program for the Science and Technology of Jilin Province (YDZJ202201ZYTS053), the Program of the Education Department of Jilin Province (No. JJKH20241338KJ) is highly appreciated.

Appendix A. Supplementary data

Supplementary data to this article can be found online at https://doi.org/10.1016/j.mtbio.2024.101256.

References

[1] E.L. Bayliss, P.A. Monk, D. Culliford, The effect of patient age at intervention on risk of implant revision after total replacement of the hip or knee: a population-based cohort study, Lancet 389 (10077) (2017) 1424–1430.
[2] D. Ke, A.A. Vu, A. Bandyopadhyay, S. Bose, Compositionally graded doped hydroxyapatite coating on titanium using laser and plasma spray deposition for bone implants, Acta Biomater. 84 (2019) 414–423.
[3] A.M. Schwartz, K.X. Farley, G.N. Guild, T.L. Bradbury, Projections and epidemiology of revision hip and knee arthroplasty in the United States to 2030, J. Arthroplasty 35.6 (2020) S79–S85.
[4] D. Tang, R.S. Tare, L.Y. Yang, D.F. Williams, R.O.C. Oreffo, Biofabrication of bone tissue: approaches, challenges and translation for bone regeneration, Biomaterials 83 (2016) 363–382.
[5] J. Song, L. Li, L. Fang, E. Zhang, Y. Zhang, Z. Zhang, P. Vangari, Y. Huang, F. Tian, Y. Zhao, Advanced strategies of scaffolds design for bone regeneration, BMEMat 1 (4) (2023) e12046.
[6] M. Janmohammadi, Z. Nazemi, A.O.M. Salehi, A. Seyfoori, J.V. John, M. S. Nourbakhsh, M. Akbari, Cellulose-based composite scaffolds for bone tissue engineering and localized drug delivery, Bioact. Mater. 20 (2023) 137–163.
[7] S.J. Wang, D. Jiang, Z.Z. Zhang, Y.R. Chen, Z.D. Yang, J.Y. Zhang, J. Shi, X. Wang, J.K. Yu, Biomimetic nanosilica–collagen scaffolds for in situ bone regeneration: toward a cell-free, one-step surgery, Adv. Mater. 31 (49) (2019) 1904341.

[8] Y. Niu, Q. Li, Y. Ding, L. Dong, C. Wang, Engineered delivery strategies for enhanced control of growth factor activities in wound healing, Adv. Drug Del. Rev. 146 (2019) 190–208.

[9] C. Wang, S. Wang, D.D. Kang, Y. Dong, Biomaterials for in situ cell therapy, BMEMat 1 (3) (2023) e12039.

[10] A.E. Jakus, A.L. Rutz, S.W. Jordan, A. Kannan, S.M. Mitchell, C. Yun, K.D. Koube, S. C. Yoo, H.E. Whiteley, C.P. Richter, Hyperelastic \"bone\": a highly versatile, growth factor-free, osteoregenerative, scalable, and surgically friendly biomaterial, Sci. Transl. Med. 8 (358) (2016), 358ra127-358ra127.

[11] X. Zhang, Y. Li, Y.E. Chen, J. Chen, P.X. Ma, Cell-free 3D scaffold with two-stage delivery of miRNA-26a to regenerate critical-sized bone defects, Nat. Commun. 7 (2016) 10376.

[12] Masahiro Omori, Shuhei Tsuchiya, Kenji Hara, Kensuke Kuroda, Hibi Hideharu, A new application of cell-free bone regeneration: immobilizing stem cells from human exfoliated deciduous teeth-conditioned medium onto titanium implants using atmospheric pressure plasma treatment, Stem Cell Res. Ther 6 (2015) 1–13.

[13] F. Lai, N. Kakudo, N. Morimoto, S. Taketani, T. Hara, T. Ogawa, K. Kusumoto, Platelet-rich plasma enhances the proliferation of human adipose stem cells through multiple signaling pathways, Stem Cell Res. Ther. 9 (1) (2018) 107.

[14] G. Fernandes, S. Yang, Application of platelet-rich plasma with stem cells in bone and periodontal tissue engineering, Bone Research 4 (1) (2016) 1–21.

[15] S. Prakash, A. Thakur, Platelet concentrates: past, present and future, J. Maxillofac. Oral Surg. 10 (1) (2011) 45–49.

[16] S. Metwally, U. Stachewicz, Surface potential and charges impact on cell responses on biomaterials interfaces for medical applications, Mater. Sci. Eng. C 104 (2019) 109883.

[17] X. Hu, S. Li, P. Peng, B. Wang, W. Liu, X. Dong, X. Yang, M. Karabaliev, Q. Yu, C. Gao, Prosthetic heart valves for transcatheter aortic valve replacement, BMEMat 1 (2) (2023) e12026.

[18] D. Khare, B. Basu, A.K. Dubey, Electrical stimulation and piezoelectric biomaterials for bone tissue engineering applications, Biomaterials 258 (2020) 120280.

[19] D.D. Kumar, G.S. Kaliaraj, A.K. Kirubaharan, K. Alagarsamy, V. Vishwakarma, R. Baskaran, Biocorrosion and biological properties of sputtered ceramic carbide coatings for biomedical applications, Surf. Coat. Technol. 374 (2019) 569–578.

[20] M. Noori, M. Atapour, F. Ashrafizadeh, H. Elmkhah, G.G. di Confiengo, S. Ferraris, S. Perero, M. Cardu, S. Spriano, Nanostructured multilayer CAE-PVD coatings based on transition metal nitrides on Ti6Al4V alloy for biomedical applications, Ceram. Int. 49 (14) (2023) 23367–23382.

[21] S. Du, K. Zhang, M. Wen, Y. Qin, R. Li, H. Jin, X. Bao, P. Ren, W. Zheng, Optimizing the tribological behavior of tantalum carbide coating for the bearing in total hip joint replacement, Vacuum 150 (2018) 222–231.

[22] Y.Y. Chang, H.L. Huang, Y.C. Chen, J.T. Hsu, T.M. Shieh, M.T. Tsai, Biological characteristics of the MG-63 human osteosarcoma cells on composite tantalum carbide/amorphous carbon films, PLoS One 9 (4) (2014) e95590.

[23] M.H. Ding, B.L. Wang, L. Li, Y.F. Zheng, A study of TaxC1−x coatings deposited on biomedical 316L stainless steel by radio-frequency magnetron sputtering, Appl. Surf. Sci. 257 (3) (2010) 696–703.

[24] Z. Wang, W. Sun, X. Xiong, H. Zhang, Z. Liu, X. Tao, Growth and properties of tantalum carbide coatings on graphite by TRD technique, Surf. Coat. Technol. 484 (2024) 130798.

[25] H. Liu, X. Zhang, J. Liu, J. Qin, Vascularization of engineered organoids, BMEMat 1 (3) (2023) e12031.

[26] C. Di, X. Yan, Y. Yang, W. Ye, M. Zhao, D. Li, Wear behaviors and high-temperature oxidation resistance properties of tantalum carbide layer, Ceram. Int. 47 (23) (2021) 32766–32774.

[27] J. Xu, L. Liu, P. Munroe, Z.-H. Xie, Promoting bone-like apatite formation on titanium alloys through nanocrystalline tantalum nitride coatings, J. Mater. Chem. B 3 (19) (2015) 4082–4094.

[28] Z.Y. Zhang, S.H. Teoh, M.S. Chong, J.T. Schantz, N.M. Fisk, M.A. Choolani, J. Chan, Superior osteogenic capacity for bone tissue engineering of fetal compared with perinatal and adult mesenchymal stem cells, Stem cells 27 (1) (2009) 126–137.

[29] Q. Yang, X. Li, H.A. Ali, S. Yu, Y. Zhang, M. Wu, S. Gao, G. Zhao, Z. Du, G. Zhang, Evaluation of suitable control genes for quantitative polymerase chain reaction analysis of maternal plasma cell-free DNA, Mol. Med. Rep. 12 (5) (2015) 7728–7734.

[30] J. Olofsson, J. Gerth, H. Nyberg, U. Wiklund, S. Jacobson, On the influence from micro topography of PVD coatings on friction behaviour, material transfer and tribofilm formation, Wear 271 (9–10) (2011) 2046–2057.

[31] C. Adelmann, J. Meersschaut, L.A. Ragnarsson, T. Conard, A. Franquet, N. Sengoku, Y. Okuno, P. Favia, H. Bender, C.e.a. Zhao, Thermally stable high effective work function TaCN thin films for metal gate electrode applications, J. Appl. Phys. 105 (5) (2009) 053516.

[32] K. Zhang, M. Wen, S. Wang, R.P. Deng, D. Gall, W.T. Zheng, Sputter deposited NbCxNy films: effect of nitrogen content on structure and mechanical and tribological properties, Surf. Coating. Technol. 258 (2014) 746–753.

[33] K. Zhang, M. Wen, Q.N. Meng, C.Q. Hu, X. Li, C. Liu, W.T. Zheng, Effects of substrate bias voltage on the microstructure, mechanical properties and tribological behavior of reactive sputtered niobium carbide films, Surf. Coating. Technol. 212 (2012) 185–191, 2012.

[34] O.Y. Khyzhun, V.A. Kolyagin, Electronic structure of cubic and rhombohedral tantalum carbonitrides studied by XPS, XES, and XAS methods, J. Electron. Spectrosc. Relat. Phenom. 137–140 (2004) 463–467.

[35] K. Zhang, M. Wen, G. Cheng, X. Li, Q.N. Meng, J.S. Lian, W.T. Zheng, Reactive magnetron sputtering deposition and characterization of niobium carbide films, Vacuum 99 (2014) 233–241.

[36] R. Chen, J.P. Tu, D.G. Liu, Y.J. Mai, C.D. Gu, Microstructure, mechanical and tribological properties of TiCN nanocomposite films deposited by DC magnetron sputtering, Surf. Coat. Technol. 205 (21–22) (2011) 5228–5234.

[37] Y. Wang, D. Zhu, X. Xu, Zr-doped mesoporous Ta3N5 microspheres for efficient photocatalytic water oxidation, ACS Appl. Mater. Inter. 8 (51) (2016) 35407–35418.

[38] C. Gao, S. Peng, P. Feng, C. Shuai, Bone biomaterials and interactions with stem cells, Bone research 5 (1) (2017) 1–33.

[39] H. Amani, H. Arzaghi, M. Bayandori, A.S. Dezfuli, H. Pazoki-Toroudi, A. Shafiee, L. Moradi, Controlling cell behavior through the design of biomaterial surfaces: a focus on surface modification techniques, Adv. Mater. Interfac. 6 (13) (2019) 1900572.

[40] S. Chen, Y. Guo, R. Liu, S. Wu, J. Fang, B. Huang, Z. Li, Z. Chen, Z. Chen, Tuning surface properties of bone biomaterials to manipulate osteoblastic cell adhesion and the signaling pathways for the enhancement of early osseointegration, Colloids Surf. B Biointerfaces 164 (2018) 58–69.

[41] B. Díaz, J. Światowska, V. Maurice, A. Seyeux, E. Härkönen, M. Ritala, S. Tervakangas, J. Kolehmainen, P. Marcus, Tantalum oxide nanocoatings prepared by atomic layer and filtered cathodic arc deposition for corrosion protection of steel: comparative surface and electrochemical analysis, Electrochim. Acta 90 (2013) 232–245.

[42] S. Leroy, H. Martinez, R. Dedryvère, D. Lemordant, D. Gonbeau, Influence of the lithium salt nature over the surface film formation on a graphite electrode in Li-ion batteries: an XPS study, Appl. Surf. Sci. 253 (11) (2007) 4895–4905.

[43] R.J. Yeo, N. Dwivedi, E. Rismani, N. Satyanarayana, S. Kundu, P.S. Goohpattader, H.R. Tan, N. Srinivasan, B. Druz, S. Tripathy, C.S. Bhatia, Enhanced tribological, corrosion, and microstructural properties of an ultrathin (<2 nm) silicon nitride/carbon bilayer overcoat for high density magnetic storage, ACS applied materials & interfaces 6 (12) (2014) 9376–9385.

[44] T. Saito, T. Hasebe, S. Yohena, Y. Matsuoka, A. Kamijo, K. Takahashi, T. Suzuki, Antithrombogenicity of fluorinated diamond-like carbon films, Diam. Relat. Mater. 14 (3–7) (2005) 1116–1119.

[45] W.-J. Chun, A. Ishikawa, H. Fujisawa, T. Takata, J.N. Kondo, M. Hara, M. Kawai, Y. Matsumoto, K. Domen, Conduction and valence band positions of Ta2O5, TaON, and Ta3N5 by UPS and electrochemical methods, J. Phys. Chem. B 107 (2003) 1798–1803.

[46] E. Yegen, A. Lippitz, D. Treu, W.E.S. Unger, Derivatization of amino groups by pentafluorobenzaldehyde (PFB) as observed by XPS and NEXAFS spectroscopy on spin coated 4,4′-methylenebis(2,6-diethylaniline) films, Surf. Interface Anal. 40 (3–4) (2008) 176–179.

[47] A.R. Balkenende, W.E.J.v. Kooten, A.R. Pieters, M. Lamers, F.J.J.G. Janssen, J. W. Geus, XPS surface characterization of a Cu/SiO 2 catalyst oxidized by NO or O 2, Appl. Surf. Sci. 68 (1993) 439–444.

[48] S. Piscanec, L.C. Ciacchi, E. Vesselli, G. Comelli, O. Sbaizero, S. Meriani, A. De Vita, Bioactivity of TiN-coated titanium implants, Acta Mater. 52 (5) (2004) 1237–1245.

[49] Y. Xie, X. Liu, P.K. Chu, C. Ding, Nucleation and growth of calcium–phosphate on Ca-implanted titanium surface, Surf. Sci. 600 (3) (2006) 651–656.

[50] K. Yamashita, N. Oikawa, T. Umegaki, Acceleration and deceleration of bone-like crystal growth on ceramic hydroxyapatite by electric poling, Chem. Mater. 8 (1996) 2697–2700.

[51] P. Fonda, Z. Wang, K. Yamazaki, Y. Akutsu, A fundamental study on Ti–6Al–4V's thermal and electrical properties and their relation to EDM productivity, J. Mater. Process. Technol. 202 (1–3) (2008) 583–589.

[52] M. Vargas, H.A. Castillo, E. Restrepo-Parra, W. De La Cruz, Stoichiometry behavior of TaN, TaCN and TaC thin films produced by magnetron sputtering, Appl. Surf. Sci. 279 (2013) 7–12.

[53] G.-C. Jun, S.-L. Cho, K.-B. Kim, H.-K. Shin, D.-H. K, Low temperature deposition of TaCN films using pentakis(diethylamido)tantalum, Jpn. J. Appl. Phys. 37 (1998) L30–L 32.

[54] X.B. Chen, Y.C. Li, P.D. Hodgson, C. Wen, The importance of particle size in porous titanium and nonporous counterparts for surface energy and its impact on apatite formation, Acta Biomater. 5 (6) (2009) 2290–2302.

[55] L. Jonášová, F.A. Müller, A. Helebrant, J. Strnad, P. Greil, Biomimetic apatite formation on chemically treated titanium, Biomaterials 25 (7–8) (2004) 1187–1194.

[56] H. Wang, Q. Zou, O.C. Boerman, A.W.G. Nijhuis, J.A. Jansen, Y. Li, S.C. G. Leeuwenburgh, Combined delivery of BMP-2 and bFGF from nanostructured colloidal gelatin gels and its effect on bone regeneration in vivo, J. Contr. Release 166 (2) (2013) 172–181.

[57] N.A. Impellitteri, M.W. Toepke, S.K.L. Levengood, W.L. Murphy, Specific VEGF sequestering and release using peptide-functionalized hydrogel microspheres, Biomaterials 33 (12) (2012) 3475–3484.

[58] J. Lee, J.J. Yoo, A. Atala, S.J. Lee, The effect of controlled release of PDGF-BB from heparin-conjugated electrospun PCL/gelatin scaffolds on cellular bioactivity and infiltration, Biomaterials 33 (28) (2012) 6709–6720.